



HAL
open science

Microstructure and mechanical properties of pure copper manufactured by selective laser melting

Xingchen Yan, Cheng Chang, Dongdong Dong, Shuohong Gao, Wenyu Ma,
Min Liu, Hanlin Liao, Shuo Yin

► To cite this version:

Xingchen Yan, Cheng Chang, Dongdong Dong, Shuohong Gao, Wenyu Ma, et al.. Microstructure and mechanical properties of pure copper manufactured by selective laser melting. *Materials Science and Engineering: A*, 2020, 789, pp.139615. 10.1016/j.msea.2020.139615 . hal-02626528

HAL Id: hal-02626528

<https://utt.hal.science/hal-02626528>

Submitted on 22 Aug 2022

HAL is a multi-disciplinary open access archive for the deposit and dissemination of scientific research documents, whether they are published or not. The documents may come from teaching and research institutions in France or abroad, or from public or private research centers.

L'archive ouverte pluridisciplinaire **HAL**, est destinée au dépôt et à la diffusion de documents scientifiques de niveau recherche, publiés ou non, émanant des établissements d'enseignement et de recherche français ou étrangers, des laboratoires publics ou privés.



Distributed under a Creative Commons Attribution - NonCommercial 4.0 International License

1 **Microstructure and mechanical properties of pure copper manufactured by selective laser melting**

2 Xingchen YAN ^{a,b}, Cheng CHANG ^{*c}, Dongdong DONG ^a, Shuohong GAO ^b, Wenyu MA ^a, Min LIU ^a, Hanlin LIAO ^b,

3 Shuo YIN ^{*d}

4 *a) National Engineering Laboratory for Modern Materials Surface Engineering Technology; The Key Lab of Guangdong for Modern*
5 *Surface Engineering Technology; Guangdong Institute of New Materials, Guangzhou 510651, P.R. China*

6 *b) ICB UMR 6303, CNRS, Univ. Bourgogne Franche-Comté, UTBM, F-90010 Belfort, France*

7 *c) ICD-LASMIS, UMR CNRS 6281, University of Technology of Troyes, 12 rue Marie Curie, CS 42060, 10004, Troyes Cedex, France*

8 *d) Trinity College Dublin, The University of Dublin, Department of Mechanical and Manufacturing Engineering, Parsons Building,*
9 *Dublin 2, Ireland*

10 **Abstract:** Selective laser melting (SLM) was used to fabricate copper samples under various processing parameters. The
11 influence of laser linear energy density on the microstructures and mechanical properties of the SLM copper samples were
12 investigated theoretically and experimentally. Based on the results, the optimal linear energy density that can result in the
13 best relative density ($99.10\pm 0.5\%$) and surface roughness ($R_a=12.72\pm 4.54\ \mu\text{m}$) was determined to be 0.50 J/mm which
14 corresponds to the laser power and scanning speed of 200 W and 400 mm/s, 300 W and 600 mm/s, respectively. Under the
15 optimal processing conditions, the microhardness and strength (i.e., yield strength and ultimate tensile strength) of the copper
16 sample achieved the highest value. In addition, it is also found that the microstructure of the SLM pure copper samples was
17 characterized by polycrystalline grains with columnar dendrites and equiaxed structures dispersed inside. The grain size
18 showed a decreasing trend as linear energy density increased due to the improved intrinsic heat treatment effect. The paper
19 proves that nearly full dense copper with desirable mechanical properties can be fabricated through SLM.

20 **Keywords:** Selective laser melting, Microstructure evolution, Mechanical property, Fracture mechanism, Roughness

1

*Corresponding authors.

E-mail addresses: Cheng CHANG: cheng.chang1993@hotmail.com, Shuo YIN: yins@tcd.ie.

21 **1 Introduction**

22 Copper (Cu) has been predominantly used as the raw material for thermal management and electrical conduction in a
23 wide range of industrial sectors due to its excellent thermal conductivity and electrical conductivity [1]. Today, the rapid
24 development of modern electronic industry has requested copper component to have complex structures [2]. Conventional
25 subtractive manufacturing technologies face a lot of challenges to fabricate such components. Thanks to the development of
26 novel additive manufacturing (AM) technology, the fabrication of copper components with complex structures has become
27 possible. Among all available AM processes, selective laser melting (SLM) has demonstrated superior advantages over other
28 processes. SLM is developed based on the discrete-stacking principle, in which a high-power laser beam is used to selectively
29 melt the powder feedstock in a powder bed according to a pre-defined computer-aided design model. The liquid molten pool
30 created by the laser rapidly cools to form a solid track which can form near-net-shape components when combined with
31 neighbouring tracks and layers. SLM offers many unique merits such as high flexibility in geometric design, rapid production
32 of components with complex geometry and high spatial resolution (e.g., porous structures, turbine disc and cellular
33 lightweight structures [3]), improved microstructure and properties [4,5], customization of products at an acceptable cost (due
34 to the lack of tooling), and little material waste through the recycling of unprocessed powder [6].

35 Despite SLM has shown great potentials as a future manufacturing technology, the working principle of SLM makes it
36 predominantly suitable for the fabrication of materials with low reflectivity, low thermal conductivity, and free of low boiling
37 point volatile elements [7], such as Fe-based alloys [8,9], Ni-based alloys [10], Co-based alloys [11], and Ti-based alloys [12].
38 However, copper and copper alloys, due to their high reflectivity and thermal conductivity, are typically not preferential raw
39 materials for SLM. As such, to date, only few studies with regard to SLM copper-based materials have been reported. Most
40 of these studies focused on the optimization of SLM processing parameters based on the principle of maximal relative density.

41 Table 1 summarizes the optimal parameters and the resultant relative densities obtained in different studies. Apart from the
 42 parameter optimization study, another important research theme is electrical conductivity of the SLM copper parts. It was
 43 reported by Zhang et al. that the SLM Cu-10Zn alloy with a relative density of 99.97 % could gain an electrical conductivity
 44 of 43.19 % ICAS [13], while in the work of Silbernagel et al. the electrical conductivity of SLM pure copper was reported to
 45 be 21.1 % ICAS in the as-fabricated state and 50.3 % in the heat-treated state (1000 °C for 4h) [14]. Very few studies also
 46 attempted to investigate the mechanical properties of SLM copper alloys. In the work of Zhang et al., the tensile strength of
 47 SLM Cu-10Zn alloy was 10 % higher than that of a forging counterpart at the expense of 25 % lower ductility [13]. A more
 48 recent study reported by Wang et al. demonstrated that SLM Cu-15Ni-8Sn alloy had better performance in both strength and
 49 ductility [15].

50 **Table 1:** Summarization of the optimal parameters and the resultant relative density of SLM copper-based materials

Key parameters	SLM machine	Relative density	Ref.
P: 1800 W, V: 300 mm/s, D: 0.14 mm.	Self-developed platform	99.97 %	[13]
P: 200 W, V: 300 mm/s, D: 0.05 mm, T: 167 μs, L: 45 μm	Renishaw AM125	85.8 %	[14]
P: 200 W, V: 100 mm/s, D: 0.05 mm T: 400 μs	Sinterstation Pro DM125	88.1 %	[16]
P: 800 W, V: 300 mm/s, L: 0.05 mm	Self-developed platform	96.6 %	[17]
P: 800 W, V: 400 mm/s, D: 0.07 mm L: 30 μm	Self-developed platform	99.4 %	[18]
P: 600 W, V: 1000 mm/s, L: 50 μm	Self-developed platform	97.8 ± 0.4 %	[19]

51 P: laser powder, V: scanning speed, D: hatch distance, T: exposure time, L: layer thickness

52 Based on the short literature review provided in the last paragraph, it can be noted that most of the existing studies,
 53 although very limited, actually focused on the processing parameter optimization of SLM copper or copper alloys, and only
 54 few attempted to explore their electrical and mechanical properties. Particularly, the mechanical properties of SLM pure

55 copper are barely reported in literature. Therefore, the current study is aimed at filling the research gap through a
56 comprehensive experimental and theoretical investigation on the macro- and micro-structure characteristics and the
57 mechanical performance of SLM copper samples.

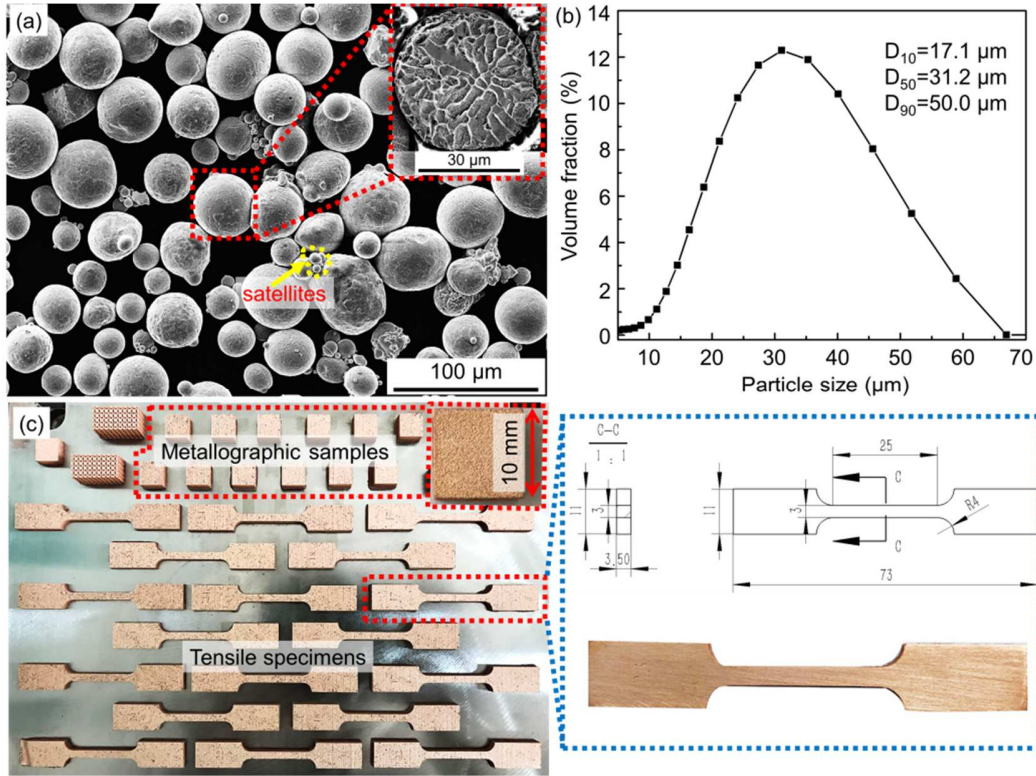
58 **2 Experimental methodology**

59 **2.1 Feedstock and processing parameters**

60 Gas-atomized pure copper powder (Beijing COMPO Advanced Technology Co.) with a minimum purity of 99.9 wt. %
61 was used as the feedstock as shown in Fig. 1a. The chemical composition of the raw materials is presented in Table 2. The
62 etched cross-sectional image of a copper powder is also presented as an insert in Fig. 1a, showing its grain structure. The
63 particle size distribution was measured using a laser diffraction particle analyzer in dry mode (Mastersizer 2000, Malvern
64 Instruments Ltd., UK), which results in $d_{10}=17.1\ \mu\text{m}$, $d_{50}=31.2\ \mu\text{m}$, and $d_{90}=50.0\ \mu\text{m}$, as indicated in Fig. 1b.

65 Cubic specimens with a dimension of 10 mm × 10 mm × 8 mm and dog-bone tensile samples with a gauge length of 25
66 mm, width of 3 mm and thickness of 3.5 mm were fabricated with an EOS M290 SLM system equipped with a 400 W
67 Yb-Fiber laser having a wavelength of 1064 nm and a laser spot size of 100 μm ($1/e^2$ value) in a Gaussian energy distribution,
68 as depicted in Fig. 1c. To avoid the oxidation of the copper samples during manufacturing, the atmosphere of the processing
69 chamber was kept as an oxidation-free environment by pumping a continuous flow of high-purity nitrogen. In order to
70 prevent the occurrence of balling phenomenon during the manufacturing process, the substrate of the building platform
71 (stainless steel grade 316L) was pre-heated to 353 K. A bi-directional scanning strategy with a rotation angle of 67° between
72 adjacent layers was applied. For finding the optimal scanning parameters, various laser power and scanning speed were
73 applied in this work. The detailed processing parameters used in this work are listed in Table 3. The reason for choosing
74 these parameters will be discussed in Section 3.1. In order to improve the ductility of the SLM copper samples, part of the

75 as-fabricated samples were annealed at a temperature of 773 K for 4 hours in vacuum environment and then air-cooled to
 76 ambient temperature (i.e., around 293 K) in atmosphere.



77
 78 **Figure 1:** (a) SEM micrograph of the copper powders used in this paper with an inserted photo showing the etched
 79 cross-section of a single particle; (b) size distribution of the powder feedstock; (c) photos of the metallographic samples and
 80 tensile specimens.

81 **Table 2:** Nominal chemical composition of the copper powders used in this study

Element	Ag	Fe	Ni	Pb	Zn	Sn	O	Cu
wt. %	0.0012	0.0005	0.0010	0.0008	0.0006	0.0240	0.0446	Balance

82

83

Table 3: Laser parameters of the SLM process applied in this study

Scanning parameters	
Laser spot diameter (μm)	100
Hatch space (μm)	80
Layer thickness (μm)	30
Laser power (W)	150, 200, 250, 300, 350
Scanning speed (mm/s)	200, 400, 600, 800, 1000

84 **2.2 Materials characterization**

85 The surface topography of the SLM samples was measured using a DektakXT profilometer (Bruker, US). The relative
 86 density of these samples was calculated based on Archimedes principle employing the following formula (1):

$$87 \quad \frac{\rho_{\text{SLM}}}{\rho_{\text{standard}}} = \frac{\rho_{\text{water}} \cdot m_{\text{SLM}(\text{air})}}{\rho_{\text{standard}} \cdot (m_{\text{SLM}(\text{air})} - m_{\text{SLM}(\text{water})})} \quad (1)$$

88 where ρ_{SLM} is the density of the SLM copper samples, ρ_{standard} is the standard density of copper [20], $m_{\text{SLM}(\text{air})}$ is the weight of
 89 the SLM samples in air, $m_{\text{SLM}(\text{water})}$ is the weight of the SLM samples in water, $\rho_{(\text{water})}$ is the density of water. The weight of
 90 the SLM parts was measured using an analytical balance (ABZ 200C, PCE instruments, Germany) and the measurement was
 91 replicated for three times to determine the mean value of the weight. Three samples were tested and averaged to determine
 92 the relative density. All the specimens for metallographic analysis were first polished using SiC grinding papers followed by
 93 Al_2O_3 suspensions. The polished cross-sections were then characterized using an optical microscope (Leica Dmi5000m,
 94 Germany) to study the defects (i.e., pores) in the sample. The polished samples were also etched by a reagent of 2 ml HCl, 1
 95 ml Fe_3Cl , and 97 ml $\text{C}_2\text{H}_5\text{OH}$ for 50 s. The microstructures were then characterized via the optical microscope and SEM (FEI
 96 Nova NanoSEM 450, US).

97 **2.3 Mechanical property tests**

98 The Vickers microhardness of the specimens was measured using a microhardness tester (Leitz-Wetzlar, Germany) with
99 a load of 50 g and a dwell time of 15 s. For each sample, ten measurements were taken from random positions on the
100 polished cross-section of the sample and averaged to obtain a mean value. Tensile tests were performed under room
101 temperature at a displacement of 10 mm/min according to the ASTM E 8M. The ultimate tensile strength (UTS) and yield
102 strength (YS) were obtained directly from the tensile tester (Instron 5982, US). The tensile strain to failure was measured
103 using strain gauges and electronic extensometers with a gauge of 10 mm. The strain gauges were fixed on the gauge region of
104 the testing sample and taken off after yielding to ensure the measurement accuracy. The elongation at break (EL) was
105 determined under the guidance of ASTM E111 standard. For each sample group, the test was replicated for three times and
106 the mean value was calculated. The fracture surfaces of the tensile samples were investigated using SEM to identify the
107 fracture mechanism of the SLM copper samples.

108 **3 Results and discussion**

109 **3.1 Processing parameter optimization**

110 **3.1.1 Theoretical calculation for the minimal linear energy density**

111 Energy density plays an important role in the manufacturing process of SLM and can be applied to roughly estimate the
112 powder melting behavior [21]. Therefore, a systematic analysis and theoretical calculation of laser parameters are conducted
113 in this section in order to determine the linear energy density required for the processing of copper via SLM. The minimal
114 energy (E_n , J/mm³) that is required to melt a unit volume of material can be expressed by Eq. (2) [22,23]:

$$115 \quad E_n = \rho[L + C_p(T_m - T_0)] \quad (2)$$

116 where ρ is the density of the copper powders, L is the latent heat of fusion, C_p is the specific heat of the bulk material, T_m is
 117 the melting point and T_0 is the initial temperature of the material before SLM processing. The physical properties of copper
 118 and the processing conditions used for copper powder during SLM can be found in Table 4. Based on Eq. 2 and Table 4, the
 119 minimum energy required for melting unit volume copper powders that has already been preheated to 353 K was calculated
 120 as 5.30 J/mm³. This suggests that the linear energy density must allow the laser energy absorbed by unit volume copper
 121 powders exceed 5.30 J/mm³ so that they can be effectively melted.

122 From the discussion above, we can note that in order to fully melt the copper powders during SLM, the laser energy
 123 absorbed by copper powders per unit volume (E_v , J/mm³) must be known and exceed 5.30 J/mm³. The following equations
 124 are thus proposed to calculate this. For facilitating the derivation, the schematics of the heat transfer process of a molten pool
 125 during SLM processing are provided in Fig. 2. We first start from the calculation of laser energy flux (q_{in} , W/mm²). If we
 126 assume that the intensity of a laser spot follows Gaussian distribution, the laser input energy flux can be expressed by Eq. (3)
 127 [24]:

$$128 \quad q_{in}(r) = \frac{2\eta P}{\pi r_b^2} \exp\left(-\frac{2r^2}{r_b^2}\right) \quad (3)$$

129 where η is the laser absorptivity coefficient of the copper powder, P is the laser power, r_b is the laser spot radius, and r is the
 130 distance from the laser center spot (also refer to Fig. 2b). By integrating Eq. 3 from 0 to r_b , we can have the total laser input
 131 energy (Q_{in} , W) as expressed by Eq. (4):

$$132 \quad Q_{in} = \int_0^{r_b} 2\pi r q_{in}(r) dr = \eta P \left(1 - \frac{1}{e^2}\right) \quad (4)$$

133 By averaging the total laser input energy over the surface area of the molten pool, we can have the average laser energy flux
 134 (q_{ave} , W/mm²) through the surface of the molten pool as expressed by Eq. (5):

135
$$q_{ave} = \frac{\eta P}{\pi r_b^2} \left(1 - \frac{1}{e^2}\right) \quad (5)$$

136 During the SLM processing of copper powders, the surface temperature of molten pool is rather high. In this respect, the
 137 laser input energy cannot be completely absorbed by the copper powders due to the high temperature induced energy loss (i.e.,
 138 convection, radiation and evaporation) as depicted in Fig. 2a. It is reported that such energy loss accounts for approximately
 139 20 % of the total laser input energy [25]. Therefore, the effective laser energy flux (q_{eff} , W/mm²) that is actually used for
 140 melting the pure copper powders can be expressed as Eq. (6):

141
$$q_{eff} = 80\%q_{ave} \quad (6)$$

142 Eqs. 5 and 6 result in the effective laser energy flux through the surface of the molten pool, from which we can further
 143 calculate the laser energy absorbed by copper powders per unit volume using Eq. (7):

144
$$E_v = \frac{\pi r_b^2 \cdot q_{eff} \cdot t}{V_{eff}} \quad (7)$$

145 where t is the laser exposure time, and V_{eff} is the effective volume of molten pool. The value of t can be determined by the
 146 formula, $t = \frac{2r_b}{v}$, where v is the laser scanning speed and $2r_b$ is the laser spot diameter. If we assume that the shape of molten
 147 pool is a segment of an equivalent sphere as displayed in Fig. 2b, the effective volume of molten pool can be estimated by Eq.
 148 (8):

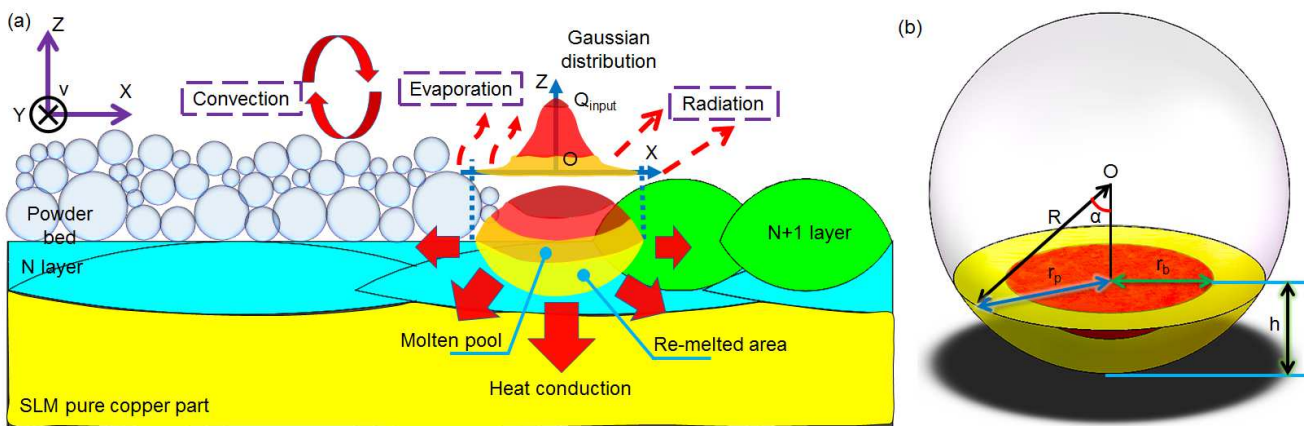
149
$$V_{eff} \cong \pi(Rh^2 - \frac{1}{3}h^3) \quad (8)$$

150 where R is the radius of the equivalent sphere, and h is the effective penetration depth of the laser in the powder bed (also
 151 refer to Fig. 2b). By substituting Eqs. 5, 6 and 8 into Eq. 7, we can find the laser energy absorbed by copper powders per unit
 152 volume during SLM as expressed in Eq. 9:

153
$$E_v = \frac{8}{5} \cdot \frac{\eta \cdot (1 - \frac{1}{e^2}) \cdot r_b}{\pi(Rh^2 - \frac{1}{3}h^3)} \cdot \frac{P}{v} \quad (9)$$

154 where $\frac{P}{v}$ is the linear energy density that can be denoted as γ .

155 The parameters that are required for solving Eq. 9 are listed in Table. 2 and also explained in Fig. 2b. Yadroitsev et al.
156 reported that the width of the continuous laser melt path was approximately 130 %-200 % of the laser spot diameter [23,26].
157 In our study, the laser spot diameter was 100 μm , and thus the width of the laser path was roughly estimated as 150 μm , half
158 of which was 75 μm (r_p). The angle of α was determined as 60° according to the measurement on the cross-section of a
159 single-track deposit from Ref [26]. R was then calculated as 86.60 μm through trigonometry. The effective melting depth of
160 the laser melting zone was calculated to be 43.30 μm from R, α and r_p as shown in Fig. 2b, where r_p is radius of laser track.
161 By solving Eq. 9 using the parameters provided in Table 4 and comparing the calculated laser energy absorbed by unit
162 volume copper powders (E_v) to the minimum linear energy density required for melting a unit volume of copper powders (E_n ,
163 5.30 J/mm³), we can find that only when the linear energy density is higher than 0.074 J/mm, the copper powders can be
164 completely melted and a continuous laser track can be formed. Therefore, all the processing parameters applied in our
165 experiments result in a linear energy density of higher than 0.074 J/mm. Therefore, the minimum linear energy density used
166 in the experiments is 0.15 J/mm in order to make sure the effective melting of copper powders.



167
168 **Figure 2:** Schematics of heat transfer process of a molten pool during SLM processing. (a) heat transfer in laser molten pool
169 during the SLM process; (b) simplified mathematical model of the laser molten pool.

170

171

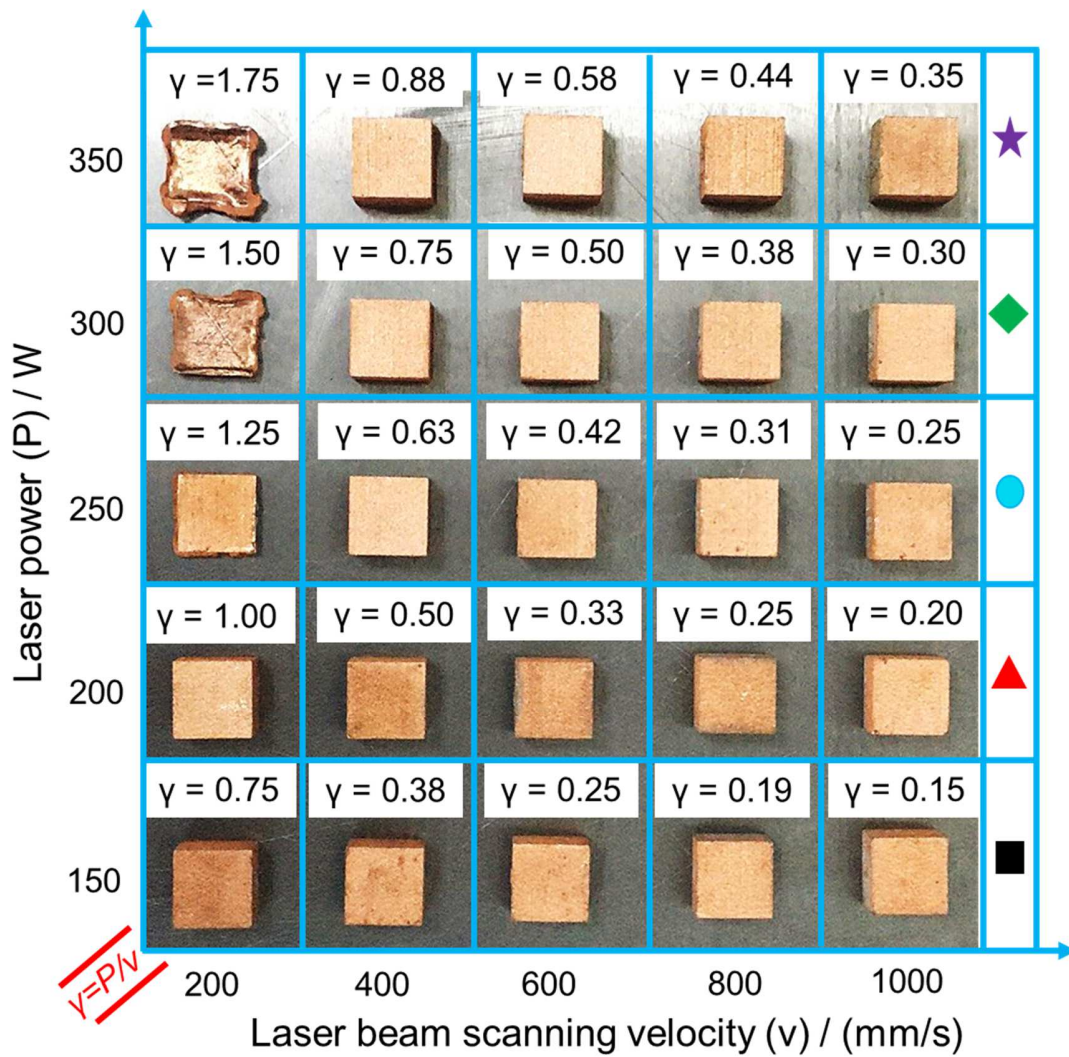
Table 4: Physical properties and process conditions of the copper powders for theoretical calculation

Physical property	Symbol	Value / unit
Density	ρ	$8.96 \times 10^3 \text{ kg/m}^3$ [20]
Specific heat	C_p	$384.6 \text{ J/(kg}\cdot\text{K)}$ [20]
Melting point	T_m	1357.77 K [20]
Initial temperature	T_0	353 K [20]
Latent heat of fusion	L	$2.05 \times 10^5 \text{ J/kg}$ [20]
Absorptivity coefficient	η	0.44 (particle size $\leq 100 \text{ }\mu\text{m}$) [27]
Laser spot radius	r_b	$50 \text{ }\mu\text{m}$
Half of the laser path	r	$75 \text{ }\mu\text{m}$

172 **3.1.2 Surface roughness**

173 Fig. 3 shows the macro morphology of the SLM copper samples fabricated under different processing parameters. It is
174 seen that all the SLM copper samples showed a perfectly cubic shape when the linear energy density was lower than 1.00
175 J/mm. Above this, the samples failed to present a cubic shape but demonstrated a distortion or collapsing feature due to the
176 excess energy input from the laser. Note that the sample made under the linear energy density of 1.25 J/mm was actually
177 distorted severely due to much higher energy input but the distortion was not clearly presented in the figure. Fig. 4 shows the
178 effect of linear energy density on the surface roughness of the samples. It is found that with increasing the linear energy
179 density the surface roughness of the SLM copper samples sharply reduced first and then increased after reaching the minimal
180 value. It is known that the surface roughness of the SLM samples is predominately affected by a so-called balling
181 phenomenon which is closely related to the linear energy density [28]. As the linear energy density increased from 0.15 to
182 0.50 J/mm, time duration of the molten pool in liquid state gradually increased, which results in an improved fluidity of the
183 molten metal. This phenomenon significantly mitigated the balling phenomenon and thus led to a reduced surface roughness
184 from $31.42 \pm 3.53 \text{ }\mu\text{m}$ to the minimum value of $12.72 \pm 4.54 \text{ }\mu\text{m}$. As the linear energy density further increased from 0.50 to

185 1.00 J/mm, the high energy led to a simultaneous melting of the copper powders and also part of previously solidified laser
 186 track, and thus an increased volume of molten pool. In this case, despite higher energy density, it is still not enough to
 187 maintain the good fluidity of the larger molten metal. Therefore, the surface roughness deteriorated after reaching the
 188 minimum value.



189
 190 **Figure 3:** Macro morphology of the SLM copper parts fabricated under different processing parameters. The linear energy
 191 density for each set of the processing parameters was calculated and provided above each sample.

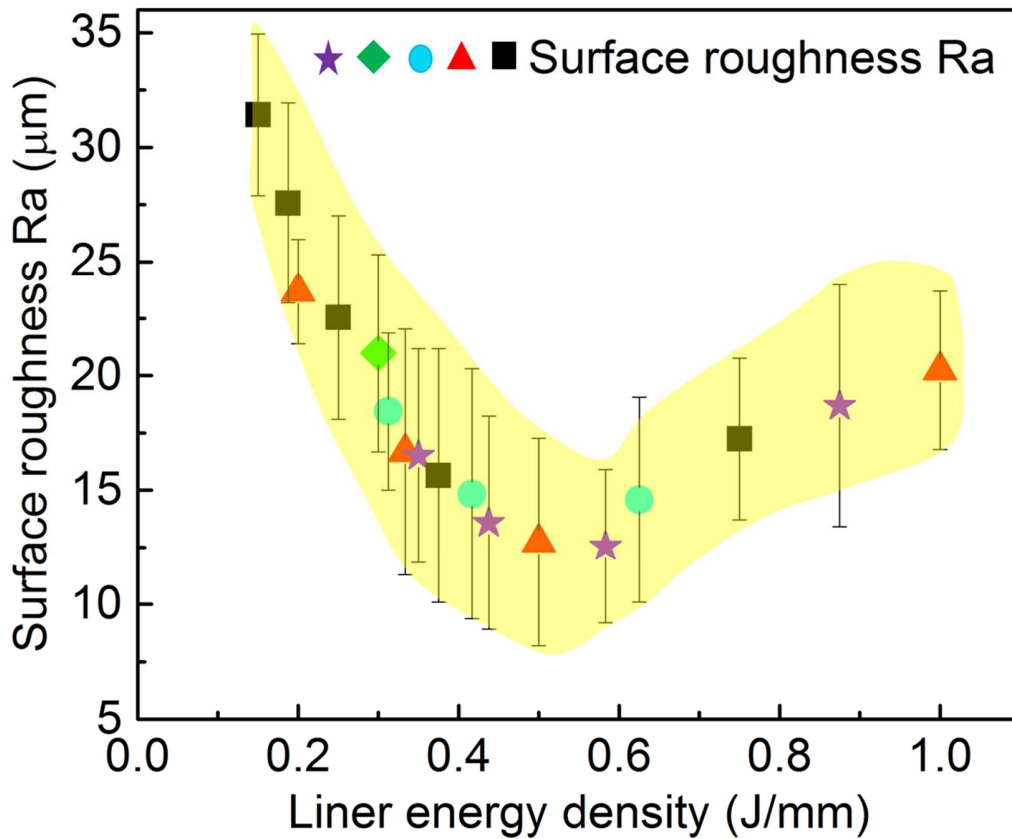
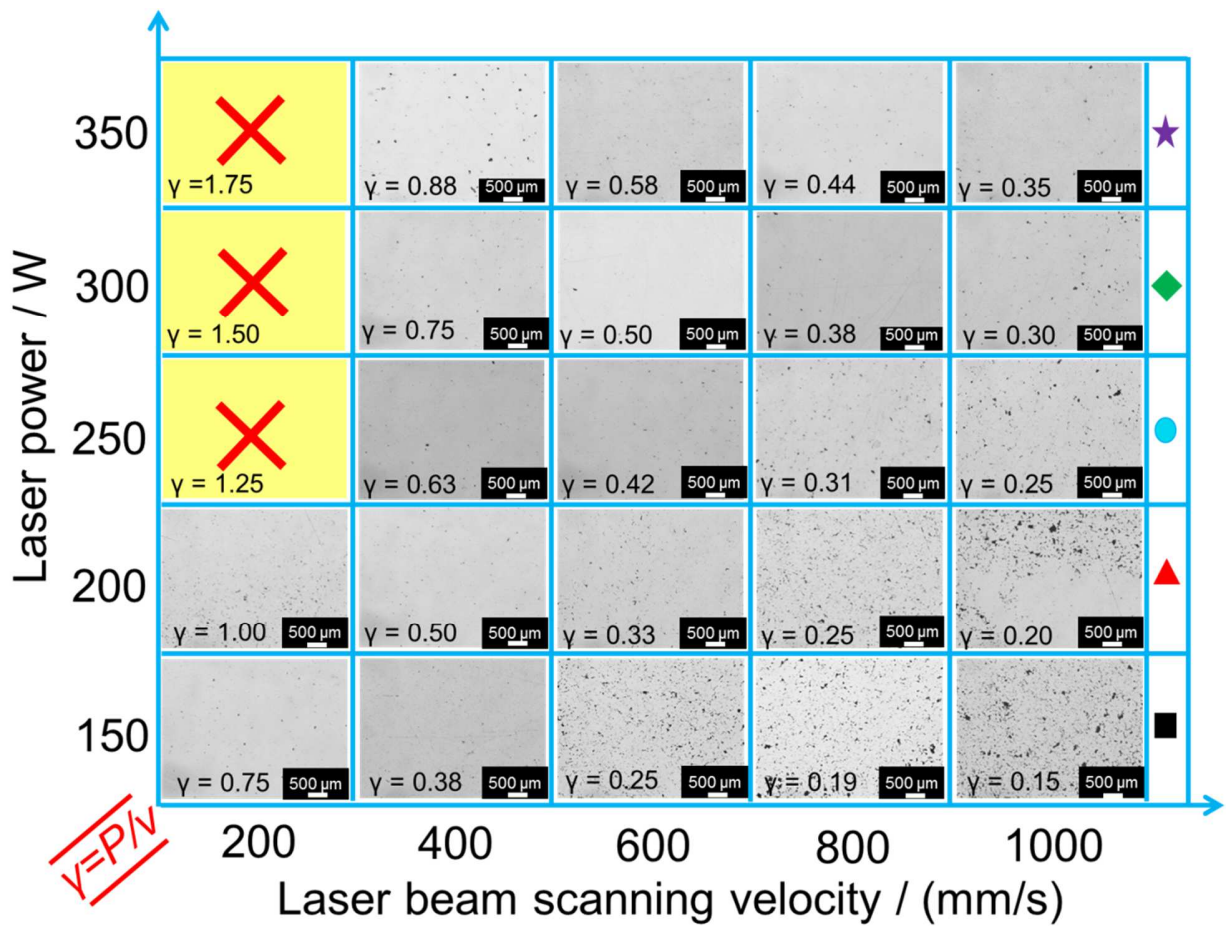


Figure 4: Effect of the liner energy density on the surface roughness

3.1.3 Relative density

Fig. 5 shows the microstructures of the SLM copper samples fabricated under different processing parameters. A large number of defects can be found when the linear energy density is at a low level (i.e., lower than $\gamma=0.5$ J/mm); such defects were significantly mitigated as the energy density increased. In order to provide a quantitative analysis, the relative density of each sample against the linear energy density is plotted in Fig. 6. It is seen that as the energy density increased the relative density rose at the beginning and then decreased after reaching the peak, which is reverse to the surface roughness changing trend. The reason for such changing trend can be summarized as follows. When the linear energy density was low (i.e., from $\gamma=0.15$ J/mm to $\gamma=0.50$ J/mm), the energy input into the molten pool was insufficient to maintain the molten pool for a long time. This resulted in a poor fluidity of the molten pool and hence the formation of irregular pores as can be seen in Fig. 5. As

203 the linear energy density increased, the fluidity of the molten pool became better and hence the porosity reduced (i.e., the
 204 relative density increased). In contrast, at higher linear energy density (i.e., from $\gamma=0.50$ J/mm to $\gamma=1.00$ J/mm), severe
 205 convective motion and vaporization of the molten pool caused a large amount of surrounding gas and reaction gas trapped in
 206 the molten pool, leading to the formation of circular pores [29]. Therefore, as the linear energy density further increased, the
 207 convective motion and vaporization of the molten metal became more prominent. As a consequence, more and more gas was
 208 trapped in the molten pool, which resulted in a reduction in relative density.



209 **Figure 5:** Microstructure of the SLM copper samples under different processing parameters.
 210

211

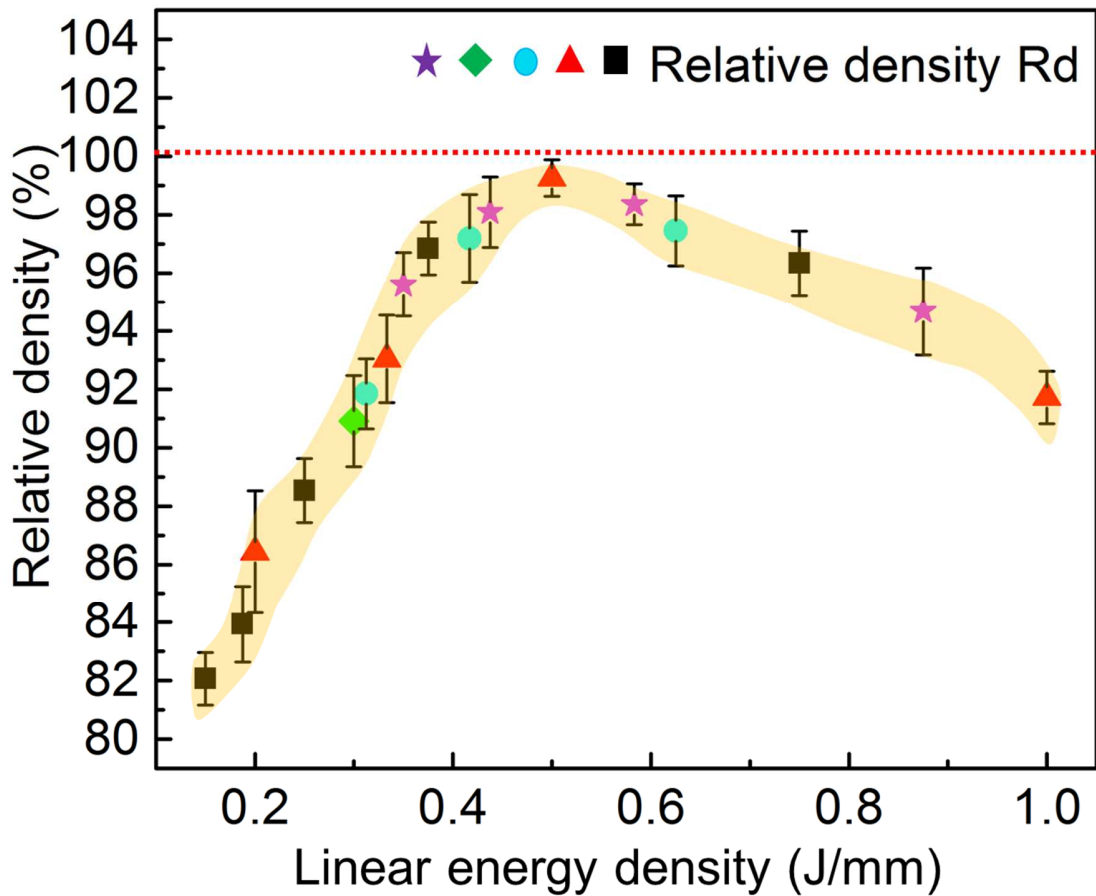
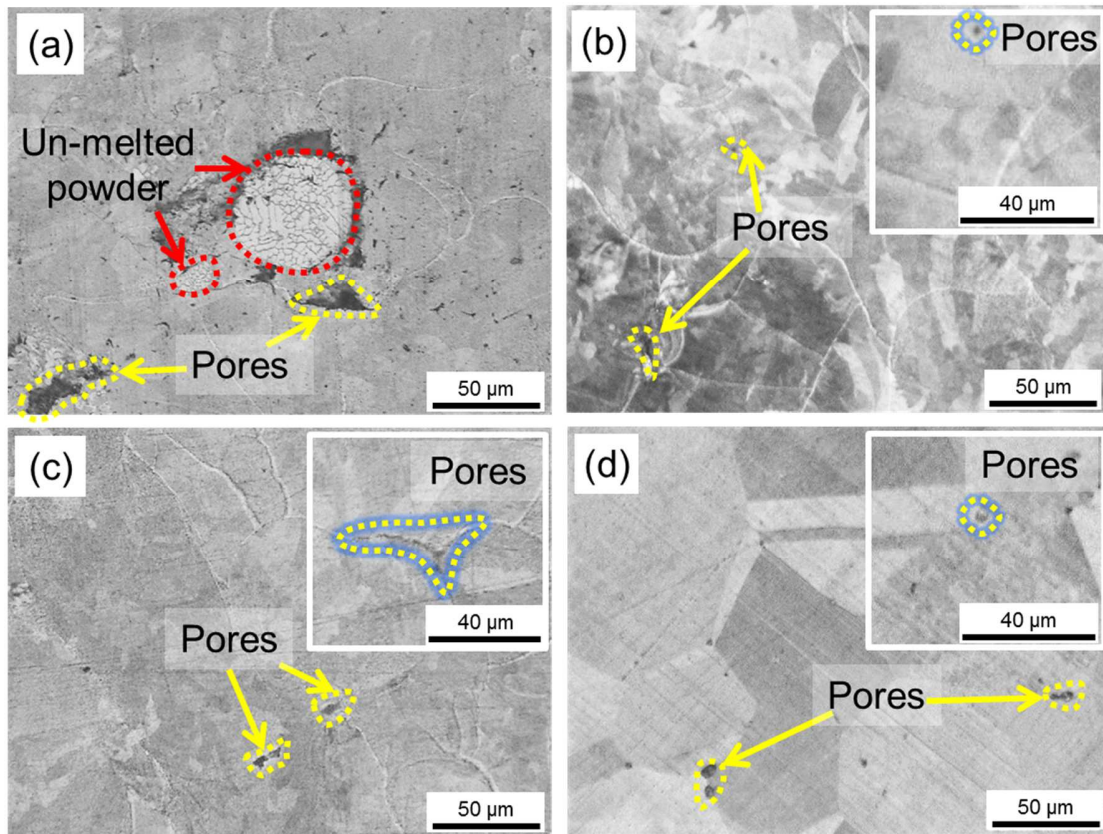


Figure 6: Effect of the liner energy density on the relative density

3.2 Microstructural evolution

Based on the results obtained from the last section, it can be found that the optimal linear energy density for the experiments performed in this work was 0.5 J/mm at which the relative density (99.10 ± 0.5 %) and surface roughness (12.72 ± 4.5 μm) achieved the optimal values. In this section, the microstructure evolution of the SLM copper sample fabricated under the optimal linear energy density was studied in the as-fabricated and heat-treated states. For comparison, two representative samples fabricated under lower ($\gamma=0.35$ J/mm) and higher ($\gamma=0.63$ J/mm) linear energy density than the optimum were also studied. Fig. 7 shows the cross-sectional microstructures of the four SLM copper samples obtained by optical microscopy.

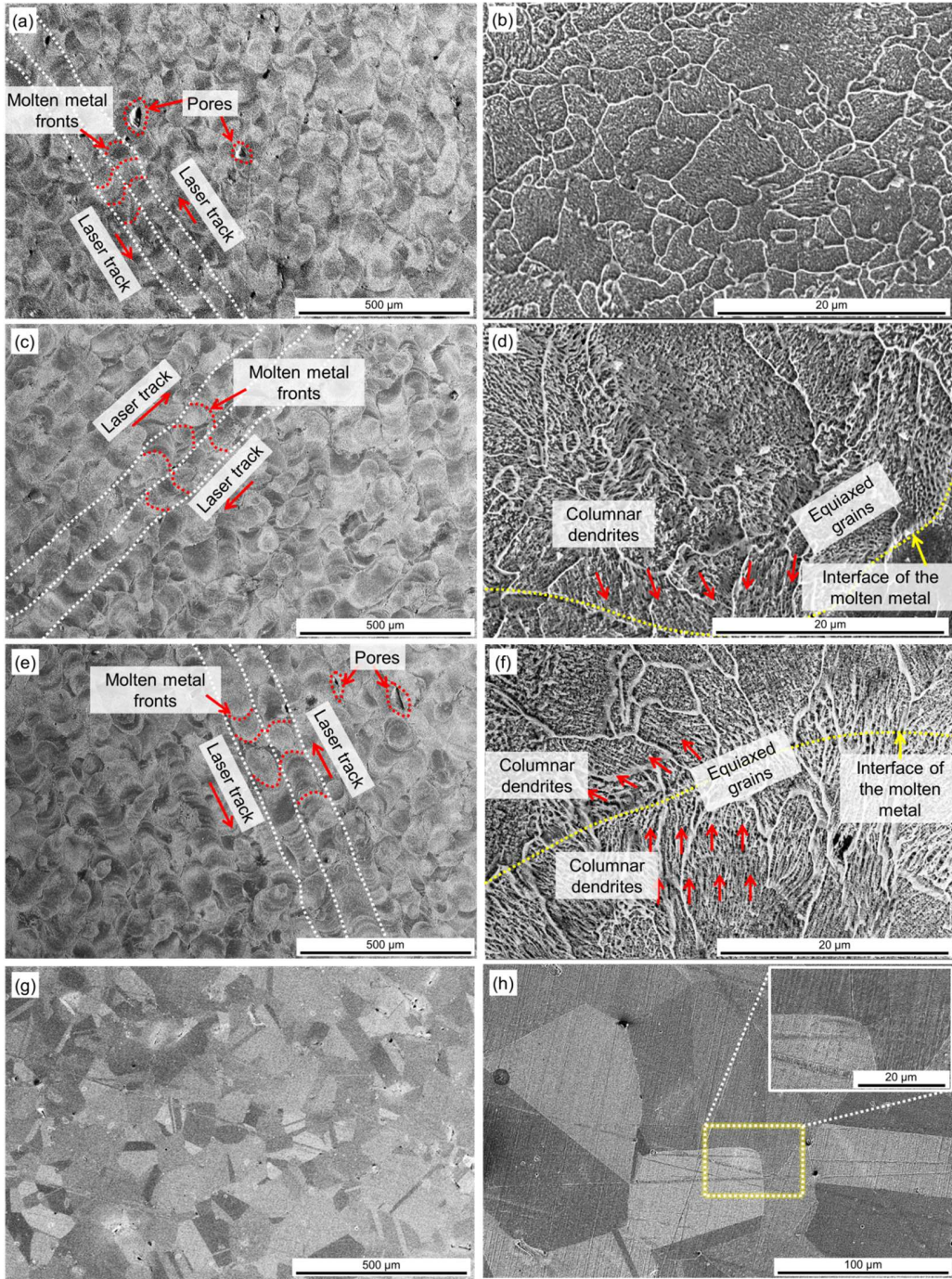
222 When the linear energy density was lower (0.35 J/mm), un-melted powders marked by the red dash lines and irregular
223 pores marked by yellow arrows were found within neighboring laser tracks as shown in Fig. 7a. This is due to the poor
224 flowability of the melted metals at the surrounding area of the fringe of the molten pool where defects tend to form. As linear
225 energy density increased to the optimal value (i.e., $\gamma=0.5$ J/mm), only a small quantity of pores were found in Fig. 7b due to
226 the optimal energy input. Further increasing the energy density to 0.63 J/mm resulted in the formation of large pores again as
227 shown in Fig. 7c due to the trapped gas. In addition, by comparing the as-fabricated sample to the heat-treated sample, the
228 latter showed a much coarser microstructure (Fig. 7d), while the character of the pores had no significant difference.



229
230 **Figure 7:** Microstructure of the SLM copper samples with different linear energy densities: (a) $\gamma=0.35$ J/mm; (b) $\gamma=0.50$
231 J/mm; (c) $\gamma=0.63$ J/mm; (d) $\gamma=0.50$ J/mm after heat treatment.

232 Fig. 8 shows the SEM images of the microstructure of the SLM copper samples fabricated under different linear energy

233 densities. The laser tracks and the molten pool fronts of different samples are clearly observed in Fig. 8a, c and e. The width
234 of the laser tracks was measured as 80-90 μm ($\gamma=0.35$ J/mm), 95-102 μm ($\gamma=0.50$ J/mm) and 100-108 μm ($\gamma=0.63$ J/mm),
235 showing an increasing trend with the energy density. These values approximately equaled to the laser spot diameter (100 μm).
236 A number of pores were found between adjacent tracks, which are consistent with the observations in Fig. 7a. In addition,
237 from the high-magnification images shown in Fig. 8b, d and f, it was found that the microstructure of the SLM copper
238 samples was characterized by columnar dendrites and equiaxed substructures distributed in polycrystalline grains. Owing to
239 the synergic effect of large thermal gradient, liquid-solid interface of the molten pool and rapid solidification rate, the
240 equiaxed structures were principally formed near the interface of the adjacent solidified molten pool fronts as marked by
241 yellow arrows shown in Figs. 8d and f, while the columnar dendrites were mainly dispersed in the polycrystalline grains.
242 Such columnar dendrites also existed in the sample fabricated under lower linear energy density ($\gamma=0.35$ J/mm), but they are
243 too small to be seen in Fig. 8b. It is also noticed that with increasing the energy density, the grains and substructures became
244 coarser and coarser due to the improved intrinsic heat treatment effect [30]. The change in grain size can be clearly seen when
245 the linear energy density was increased from 0.35 to 0.50 J/mm (Figs. 8b and d). With further increasing the linear energy
246 density, the variation in grain size is not prominent but the substructures (i.e., columnar dendrites) became larger (Figs. 8d
247 and f). Furthermore, by comparing the as-fabricated sample to the heat-treated sample, it was seen that the grains grew to a
248 larger size after heat treatment due to the recrystallization phenomenon, and the substructures (i.e., columnar dendrites and
249 equiaxed structures) vanished as depicted in Fig. 8g.



250

251

252

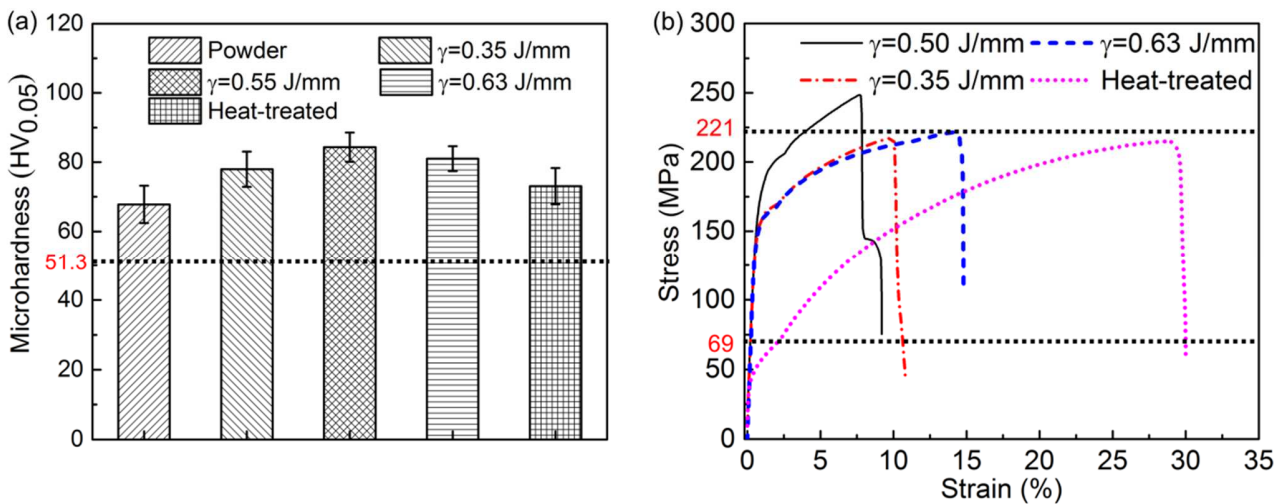
253

Figure 8: SEM images showing the microstructures of the SLM copper samples fabricated under different linear energy densities. (a, b) $\gamma=0.35$ J/mm, (c, d) $\gamma=0.50$ J/mm, (e, f) $\gamma=0.63$ J/mm, (g, h) $\gamma=0.50$ J/mm after heat treatment. Left column: low magnification images, right column: high magnification images.

254 **3.3 Mechanical properties**

255 **3.3.1 Microhardness and tensile performances**

256 The microhardness and the stress-strain curves of the SLM copper samples fabricated under different linear energy
257 densities are shown in Fig. 9, and the corresponding statistic data is provided in Table 5. For comparison, the microhardness
258 of the copper powder used in this work and a wrought C11000 copper counterpart is provided in Fig. 9a as well. It is seen in
259 Fig. 9a that the copper sample fabricated under the optimal linear energy density ($\gamma=0.50$ J/mm) had the highest
260 microhardness due to the least microstructural defects and highest relative density among the three samples. Furthermore, the
261 microhardness of the SLM copper samples was higher than that of the powders because of the finer grain structures caused
262 by the much higher cooling rate experienced by the copper samples during (10^5 - 10^6 K/s [31]) than that experienced by the
263 powders during gas atomization (10^4 - 10^5 K/s [32]). For the same reason, the microhardness of the SLM copper sample was
264 64 % higher than that of the wrought C11000 copper. In addition, after heat treatment, due to the occurrence of
265 recrystallization-induced grain size growth, the microhardness showed a 13 % reduction.



266

267

Figure 9. Mechanical properties of the SLM pure copper sample. (a) microhardness, and (b) stress-strain curves

268 As for the tensile test, the SLM copper samples exhibited excellent mechanical properties due to the fine grains caused
 269 by extremely rapid cooling. Again, the copper sample fabricated under the optimal linear energy density had the highest YS
 270 and UTS due to the least microstructural defects. The EL of the copper samples had no significant difference as the linear
 271 energy density increased from 0.35 to the optimum ($\gamma=0.50$ J/mm). Despite a slight decrease, such change can be reasonably
 272 neglected by considering the error bars. It is not clear why EL was not improved under the synergistic effect of increased
 273 relative density and grain size at the optimal condition. Further in-depth investigations are needed to fully clarify this. For
 274 higher linear energy density, a 57 % increase of EL was found as compared to the optimum ($\gamma=0.5$ J/mm). This may be due to
 275 the increased grain size which contributes to the improvement of ductility. When comparing the mechanical properties of the
 276 SLM samples with the wrought C11000 copper (YS=69-365 MPa, UTS=221-455 MPa [20]), it was found that the YS of the
 277 SLM copper samples was 28 % ($\gamma=0.35$ J/mm), 71 % ($\gamma=0.50$ J/mm) and 22 % ($\gamma=0.63$ J/mm) higher than the lower
 278 threshold of the YS of the wrought copper. The UTS of the SLM copper samples fabricated under optimal linear energy
 279 density ($\gamma=0.50$ J/mm) was 27 MPa higher than the lower threshold of C11000 copper, while the other two samples had
 280 equivalent values. The EL of all the SLM copper samples was much higher than the lower threshold of C11000 copper. The
 281 comparison clearly demonstrated that the SLM copper samples fabricated in this work can meet the minimum requirement of
 282 wrought parts. In addition, the mechanical properties of the heat-treated sample were also compared with those of the
 283 as-fabricated sample. After heat treatment, the YS and UTS showed a sharp decrease by approximately 27 % due to the
 284 recrystallization-induced grain coarsening. For the same reason, a significant improvement of ductility by 226 % was found
 285 for the heat-treated sample.

286 **Table 5:** Mechanical properties of the SLM copper samples

Samples	Microhardness (HV _{0.05})	YS (MPa)	UTS (MPa)	EL (%)
$\gamma=0.35$ J/mm	78±5.1	157±7.1	218±10.0	10.8±1.25

$\gamma=0.50$ J/mm	84±4.2	187±5.3	248±8.5	9.2±2.12
$\gamma=0.63$ J/mm	81±3.6	153±6.9	222±9.3	14.8±1.75
$\gamma=0.50$ J/mm (heat-treated)	73±5.2	51±8.2	215±7.2	30.0±3.04
Powder	68±5.4	--	--	--
C11000 [20]	51.3-104	69-365	221-455	4-55

287 3.3.2 Fracture mechanism

288 Fig. 10 shows the fractography of the SLM copper samples fabricated under different energy densities after tensile test.

289 It was found from Fig. 10a, c and e that the tensile samples in the as-fabricated state did not exhibit an obvious necking

290 phenomenon, showing a brittle fracture feature. From the high-magnification views shown in Fig. 10b, d, and f, both

291 dimple-like and river-like features can be clearly seen on the fracture surfaces, which confirms that the fracture mode for the

292 as-fabricated SLM copper samples was not a single mode but a mixed ductile-brittle mode. It was also seen that large voids

293 were formed on the fracture surface of the sample fabricated under the energy density of 0.35 J/mm. Such voids were the

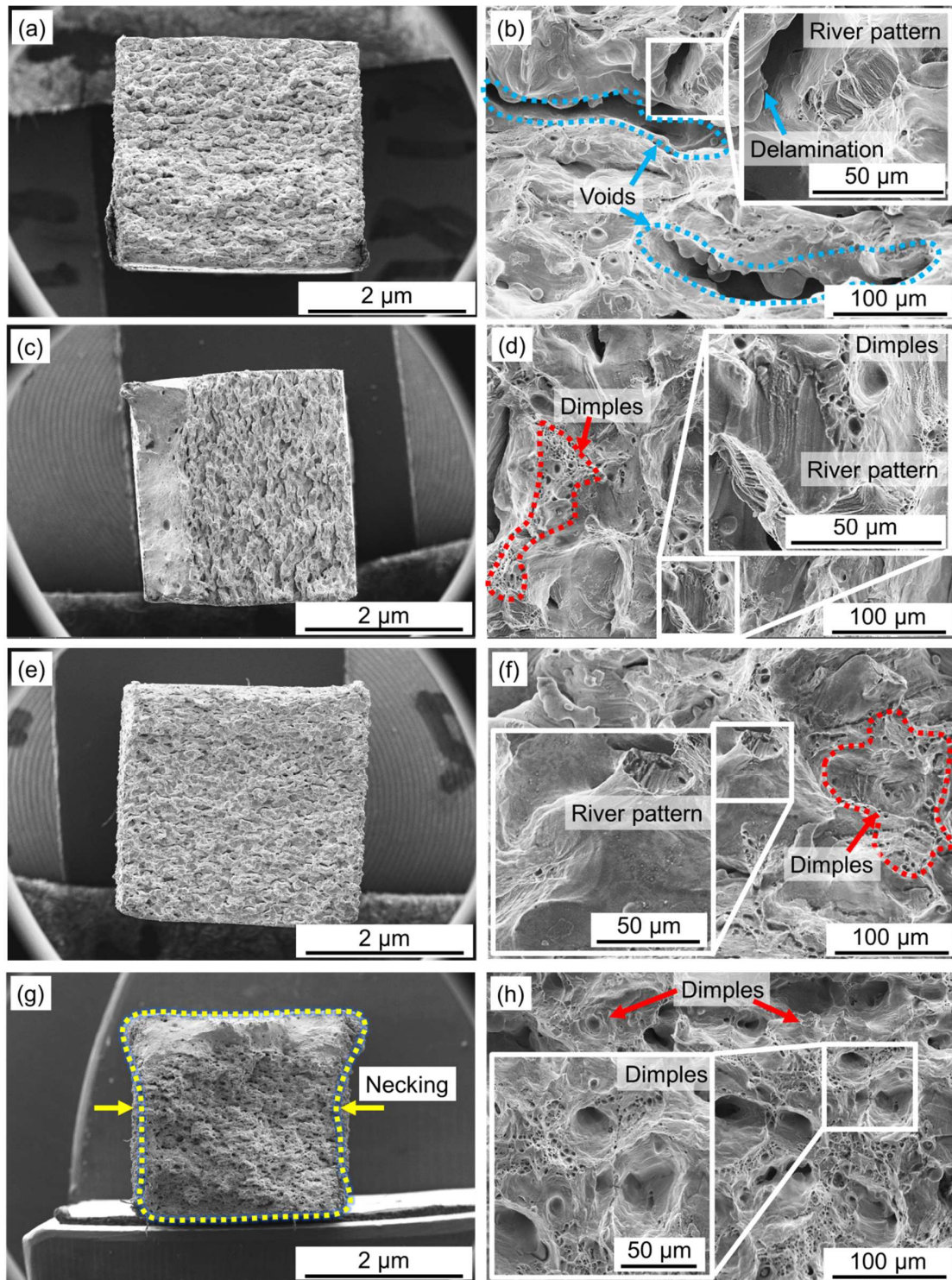
294 pores that can be seen on the cross-section of the sample as shown in Figs. 7a and 8a, which were rather detrimental to the

295 mechanical property. However, for the heat-treated sample, necking phenomenon marked by yellow dashed line was clearly

296 observed as shown in Fig. 10g, suggesting the occurrence of ductile fracture. This was further confirmed by the

297 high-magnification fractography shown in Fig. 10h where many large dimples were found randomly distributed on the

298 fracture surface.



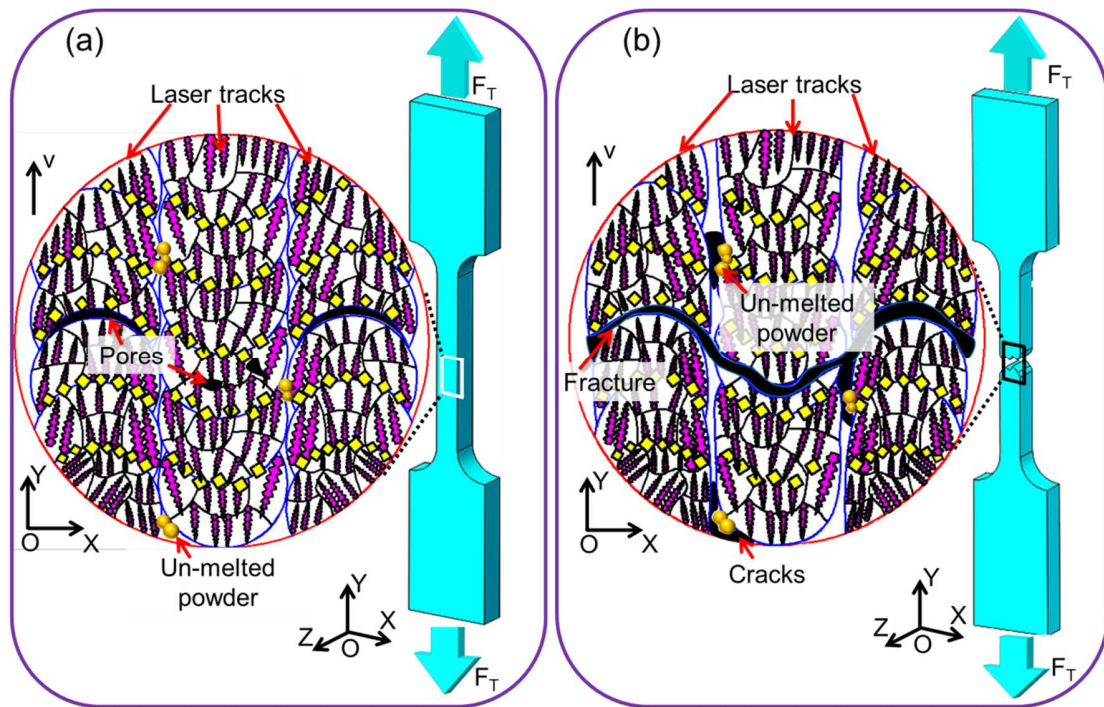
299

300 **Figure 10:** Fractography of the SLM the copper samples fabricated under different linear energy densities after tensile test. (a,

301 b) $\gamma=0.35$ J/mm, (c, d) $\gamma=0.50$ J/mm, (e, f) $\gamma=0.63$ J/mm, (g, h) $\gamma=0.50$ J/mm after heat treatment. Left column: low

302 magnification images, right column: high magnification images.

303 Fig. 11 describes the relationship between the microstructure and tensile behavior of the SLM copper samples before
304 and after the tensile test. Due to the high melting point and excellent thermal conductivity of copper, the solidification rate of
305 the copper molten pool is extremely high. Therefore, when the linear energy density was low ($\gamma=0.35$ J/mm), defects (i.e.,
306 incompletely melted powders and pores) tended to form within the adjacent region of two laser track as can be seen in Figs
307 7a and 8a. Such defects were preferential locations for the generation of stress concentration and initiation of cracks which
308 then developed to cause the fracture of the tensile samples as illustrated in Fig. 11b [31]. Therefore, large voids were clearly
309 observed on the fractures surface of the sample fabricated under lower linear energy density as shown in Fig. 10b. When the
310 optimal linear energy density ($\gamma=0.50$ J/mm) was applied, pores and un-melted powders were significantly mitigated. In this
311 case, stress concentration was more likely to occur at the surrounding area of molten pool front where a large number of
312 columnar dendrites were formed as also illustrated in Fig. 11b. Under higher linear energy density ($\gamma=0.63$ J/mm), porosity
313 and the size of columnar dendrites both increased, which worked together to induce the stress concentration and crack
314 initiation. After heat treatment, residual strain and stress were released and grains grew due to the recrystallization, and the
315 possible poor bond between adjacent laser tracks can be significantly improved though diffusion. The microstructure of the
316 heat-treated sample was very similar to that of a wrought counterpart [20]. Therefore, the fracture mechanism shall be similar
317 to that for a wrought counterpart.



318

319 **Figure 11:** Schematics showing the relationship between the microstructure and tensile behavior of the SLM copper samples.

320

(a) before tensile test; (b) after tensile test.

321 4 Conclusions

322 In summary, copper samples were successfully fabricated through SLM technology in this work to study the effect of
 323 laser linear energy density on their microstructure and mechanical properties. Based on the results and discussion, the main
 324 conclusions are listed as follows:

- 325 1. The theoretical approach proposed in this work can be used to estimate the minimal linear laser energy density that is
 326 required to melt the copper powders. The value was determined to be 0.074 J/mm in this work.
- 327 2. The parameter optimization experiments demonstrated that the optimal linear energy density for this study was 0.50 J/mm
 328 which can result in the best relative density of $99.10 \pm 0.5\%$ and surface roughness of $Ra = 12.72 \pm 4.5 \mu\text{m}$.
- 329 3. The microstructure of the SLM copper samples was characterized by polycrystalline grains with columnar dendrites and

330 equiaxed structures dispersed inside. The grain size showed a decreasing trend as linear energy density increased due to the
331 improved intrinsic heat treatment effect. Heat treatment was found to significantly increase the grain size of the SLM copper
332 sample due to the occurrence of recrystallization.

333 4. Under the optimal linear energy density, the microhardness and strength (i.e., YS and UTS) of the copper sample achieved
334 the highest value. The mechanical properties of the sample meet the minimum requirement of wrought parts. After heat
335 treatment, the YS and UTS showed a sharp decrease due to the recrystallization-induced grain coarsening, while the ductility
336 improved significantly.

337 **Acknowledgement**

338 Dr. Xingchen Yan is grateful for the financial support from Sciences Platform Environment and Capacity Building
339 Projects of GDAS (2019GDASYL-0402004, 2019GDASYL-0502006, 2020GDASYL-20200103108,
340 2019GDASYL-0402006, 2020GDASYL-20200402005, 2018GDASCX-0402, 2018GDASCX-0111 and
341 2019GDASYL-0501009), Guangzhou Project of Science & Technology (201909010008, 201807010030), Guangdong
342 province Science and Technology Plan Projects (2019A1515011841, 2017A070701027, 2017A070702016,
343 2014B070705007 and 2017B030314122). Mr. Cheng Chang would like to thank the support from China Scholarship Council
344 (201801810106).

345 **References**

- 346 [1] Copper as electrical conductive material with above-standard performance properties, (2015) 1–38.
347 <http://www.conductivity-app.org/single-article/cu-overview#L15>.
- 348 [2] P.X. Jiang, M.H. Fan, G.S. Si, Z.P. Ren, Thermal-hydraulic performance of small scale micro-channel and
349 porous-media heat-exchangers, *Int. J. Heat Mass Transf.* 44 (2001) 1039–1051.
350 doi:10.1016/S0017-9310(00)00169-1.

- 351 [3] X. Yan, Q. Li, S. Yin, Z. Chen, R. Jenkins, C. Chen, J. Wang, W. Ma, R. Bolot, R. Lupoi, Z. Ren, H. Liao, M. Liu,
352 Mechanical and in vitro study of an isotropic Ti6Al4V lattice structure fabricated using selective laser melting, *J.*
353 *Alloys Compd.* 782 (2019) 209–223. doi:10.1016/j.jallcom.2018.12.220.
- 354 [4] X. Yan, S. Yin, C. Chen, C. Huang, R. Bolot, R. Lupoi, M. Kuang, W. Ma, C. Coddet, H. Liao, M. Liu, Effect of heat
355 treatment on the phase transformation and mechanical properties of Ti6Al4V fabricated by selective laser melting, *J.*
356 *Alloys Compd.* 764 (2018) 1056–1071. doi:10.1016/j.jallcom.2018.06.076.
- 357 [5] X. Yan, S. Yin, C. Chen, R. Jenkins, R. Lupoi, R. Bolot, W. Ma, M. Kuang, H. Liao, J. Lu, M. Liu, Fatigue strength
358 improvement of selective laser melted Ti6Al4V using ultrasonic surface mechanical attrition, *Mater. Res. Lett.* 7
359 (2019) 327–333. doi:10.1080/21663831.2019.1609110.
- 360 [6] X. Yan, C. Chen, R. Zhao, W. Ma, R. Bolot, J. Wang, Z. Ren, H. Liao, M. Liu, Selective laser melting of WC
361 reinforced maraging steel 300: Microstructure characterization and tribological performance, *Surf. Coatings Technol.*
362 371 (2019) 355–365. doi:10.1016/j.surfcoat.2018.11.033.
- 363 [7] C. Yang, Y.J. Zhao, L.M. Kang, D.D. Li, W.W. Zhang, L.C. Zhang, High-strength silicon brass manufactured by
364 selective laser melting, *Mater. Lett.* 210 (2018) 169–172. doi:10.1016/j.matlet.2017.09.011.
- 365 [8] X. Yan, C. Chen, C. Chang, D. Dong, R. Zhao, R. Jenkins, J. Wang, Z. Ren, M. Liu, H. Liao, R. Lupoi, Study of the
366 microstructure and mechanical performance of C-X stainless steel processed by selective laser melting (SLM),
367 *Mater. Sci. Eng. A.* 781 (2020) 139227. doi:10.1016/j.msea.2020.139227.
- 368 [9] C. Chang, X. Yan, R. Bolot, J. Gardan, S. Gao, Influence of post-heat treatments on the mechanical properties of CX
369 stainless steel fabricated by selective laser melting, *J. Mater. Sci.* (2020) 1–14. doi:10.1007/s10853-020-04566-x.
- 370 [10] H. Zhang, D. Gu, L. Xi, H. Zhang, M. Xia, C. Ma, Anisotropic corrosion resistance of TiC reinforced Ni-based
371 composites fabricated by selective laser melting, *J. Mater. Sci. Technol.* 35 (2019) 1128–1136.
372 doi:10.1016/j.jmst.2018.12.020.
- 373 [11] Y. Lu, X. Xu, C. Yang, L. Ren, K. Luo, K. Yang, J. Lin, In vitro insights into the role of copper ions released from
374 selective laser melted CoCrW-xCu alloys in the potential attenuation of inflammation and osteoclastogenesis, *J.*
375 *Mater. Sci. Technol.* (2019) 163245. doi:10.1016/j.ijleo.2019.163245.

- 376 [12] X. Yan, R. Lupoi, H. Wu, W. Ma, M. Liu, G. O'Donnell, S. Yin, Effect of hot isostatic pressing (HIP) treatment on
377 the compressive properties of Ti6Al4V lattice structure fabricated by selective laser melting, *Mater. Lett.* 255 (2019)
378 126537. doi:10.1016/j.matlet.2019.126537.
- 379 [13] S. Zhang, H. Zhu, Z. Hu, X. Zeng, F. Zhong, Selective Laser Melting of Cu-10Zn alloy powder using high laser
380 power, *Powder Technol.* 342 (2019) 613–620. doi:10.1016/j.powtec.2018.10.002.
- 381 [14] C. Silbernagel, L. Gargalis, I. Ashcroft, R. Hague, M. Galea, P. Dickens, Electrical resistivity of pure copper
382 processed by medium-powered laser powder bed fusion additive manufacturing for use in electromagnetic
383 applications, *Addit. Manuf.* 29 (2019) 100831. doi:10.1016/j.addma.2019.100831.
- 384 [15] J. Wang, X.L. Zhou, J. Li, M. Brochu, Y.F. Zhao, Microstructures and properties of SLM-manufactured
385 Cu-15Ni-8Sn alloy, *Addit. Manuf.* 31 (2020) 100921. doi:10.1016/j.addma.2019.100921.
- 386 [16] P.A. Lykov, E. V. Safonov, A.M. Akhmedianov, Selective laser melting of copper, *Mater. Sci. Forum.* 843 (2016)
387 284–288. doi:10.4028/www.scientific.net/MSF.843.284.
- 388 [17] T.T. Ikeshoji, K. Nakamura, M. Yonehara, K. Imai, H. Kyogoku, Selective Laser Melting of Pure Copper, *Jom.* 70
389 (2018) 396–400. doi:10.1007/s11837-017-2695-x.
- 390 [18] S.D. Jadhav, S. Dadbakhsh, L. Goossens, J.P. Kruth, J. Van Humbeeck, K. Vanmeensel, Influence of selective laser
391 melting process parameters on texture evolution in pure copper, *J. Mater. Process. Technol.* 270 (2019) 47–58.
392 doi:10.1016/j.jmatprotec.2019.02.022.
- 393 [19] M. Colopi, L. Caprio, A.G. Demir, B. Previtali, Selective laser melting of pure Cu with a 1 kW single mode fiber
394 laser, *Procedia CIRP.* 74 (2018) 59–63. doi:10.1016/j.procir.2018.08.030.
- 395 [20] ASM International Handbook Committee, *ASM Speciality Handbook, Copper and Copper Alloys*, 2001.
- 396 [21] K.G. Prashanth, S. Scudino, T. Maity, J. Das, J. Eckert, Is the energy density a reliable parameter for materials
397 synthesis by selective laser melting?, *Mater. Res. Lett.* 5 (2017) 386–390. doi:10.1080/21663831.2017.1299808.
- 398 [22] W.M. Steen, J. Mazumder, *Laser Material Processing*, Springer Science & Business Media, 2010.
399 <http://medcontent.metapress.com/index/A65RM03P4874243N.pdf>.
- 400 [23] I. Yadroitsev, P. Krakhmalev, I. Yadroitsava, S. Johansson, I. Smurov, Energy input effect on morphology and

- 401 microstructure of selective laser melting single track from metallic powder, *J. Mater. Process. Technol.* 213 (2013)
402 606–613. doi:10.1016/j.jmatprotec.2012.11.014.
- 403 [24] L. Han, F.W. Liou, S. Musti, Thermal behavior and geometry model of melt pool in laser material process, *J. Heat*
404 *Transfer.* 127 (2005) 1005–1014. doi:10.1115/1.2005275.
- 405 [25] X. He, J. Mazumder, Transport phenomena during direct metal deposition, *J. Appl. Phys.* 101 (2007).
406 doi:10.1063/1.2710780.
- 407 [26] I. Yadroitsev, I. Shishkovsky, P. Bertrand, I. Smurov, Manufacturing of fine-structured 3D porous filter elements by
408 selective laser melting, *Appl. Surf. Sci.* 255 (2009) 5523–5527. doi:10.1016/j.apsusc.2008.07.154.
- 409 [27] Y. Shenping, Z. Anfeng, L. Shaoduan, W. Tan, Measurement of Laser Light Absorptivity of Commonly Used Metals
410 in Laser Additive Manufacturing Technique, *Aeronaut. Manuf. Technol.* (2017) 97–100.
411 doi:10.16080/j.issn1671-833x.2017.17.097.
- 412 [28] X. Zhou, X. Liu, D. Zhang, Z. Shen, W. Liu, Balling phenomena in selective laser melted tungsten, *J. Mater. Process.*
413 *Technol.* 222 (2015) 33–42. doi:10.1016/j.jmatprotec.2015.02.032.
- 414 [29] W.E. King, H.D. Barth, V.M. Castillo, G.F. Gallegos, J.W. Gibbs, D.E. Hahn, C. Kamath, A.M. Rubenchik,
415 Observation of keyhole-mode laser melting in laser powder-bed fusion additive manufacturing, *J. Mater. Process.*
416 *Technol.* 214 (2014) 2915–2925. doi:10.1016/j.jmatprotec.2014.06.005.
- 417 [30] J. Haubrich, J. Gussone, P. Barriobero-Vila, P. Kürsteiner, E.A. Jägler, D. Raabe, N. Schell, G. Requena, The role of
418 lattice defects, element partitioning and intrinsic heat effects on the microstructure in selective laser melted
419 Ti-6Al-4V, *Acta Mater.* 167 (2019) 136–148. doi:10.1016/j.actamat.2019.01.039.
- 420 [31] J.H. Martin, B.D. Yahata, J.M. Hundley, J.A. Mayer, T.A. Schaedler, T.M. Pollock, 3D printing of high-strength
421 aluminium alloys, *Nature.* 549 (2017) 365–369. doi:10.1038/nature23894.
- 422 [32] C. Si, X. Tang, X. Zhang, J. Wang, W. Wu, Characteristics of 7055Al alloy powders manufactured by gas-solid
423 two-phase atomization: A comparison with gas atomization process, *Mater. Des.* 118 (2017) 66–74.
424 doi:10.1016/j.matdes.2017.01.028.